Dynamic decoupling of salience and default mode networks by optogenetic manipulation of anterior insular cortex

Vinod Menon[1,*,a,b,c], *Domenic Cerri*[1,d,e,f], *Byeongwook Lee*[1,a], *Rui Yuan*[a], *Sung-Ho Lee*[d,e,f], *Yen-Yu Ian Shih*[*,d,e,f]

Department of Psychiatry & Behavioral Sciences[a]
Department of Neurology & Neurological Sciences[b]
Stanford Neurosciences Institute[c]
Stanford University School of Medicine
Stanford, CA 94305

Center for Animal MRI[d]
Biomedical Research Imaging Center[e]
Department of Neurology[f]
University of North Carolina at Chapel Hill
Chapel Hill, NC 27599

Please address correspondence to: *Vinod Menon, Ph.D., *Ian Shih, Ph.D.
Email: menon@stanford.edu, shihy@unc.edu

Author Contributions:
[1]*Denotes equal first-author contribution.*
V.M., D.C., and Y.Y.I.S. designed research; D.C., B.L., and R.Y. performed research; V.M., D.C., B.L., R.Y. and S.H.L. analyzed data; and V.M., D.C., B.L., and Y.Y.I.S. wrote the paper.

Keywords: Optogenetics, Default Mode Network, Salience Network, fMRI, Anterior Insular Cortex, Functional Connectivity, Computational Modeling, Bayesian, Hidden Markov Model, Retrosplenial Cortex, Medial Prefrontal Cortex, Cingulate Cortex, Prelimbic Cortex

Abstract

The salience network (SN) and default mode network (DMN) are among the most widely investigated networks in the human brain. The SN, anchored in the anterior insular cortex (AI), is thought to play a critical role in stimulus-driven suppression of DMN nodes. However, the causal neural mechanisms underlying DMN suppression and SN-DMN interactions are poorly understood. Here we combine feedforward optogenetic AI stimulation with fMRI and computational modeling to dissect the causal role of AI in dynamic functional interactions between SN and DMN nodes in the rat brain. Optogenetic stimulation of Chronos-expressing AI neurons in rats suppressed DMN activity and decreased AI-DMN and intra-DMN functional connectivity. Our findings demonstrate that feedforward optogenetic stimulation of AI neurons induces dynamic suppression and decoupling of the DMN and elucidates previously unknown features of rodent brain network organization. Our study advances foundational knowledge of causal mechanisms underlying dynamic cross-network interactions and brain network switching.

Introduction

Dynamic interactions between the salience network (SN) and default mode network (DMN) play a critical role in human brain function and dysfunction (1, 2). First identified from imaging data on the basis of task-related profiles of activation and deactivation during behavior, the SN is activated during attentionally demanding tasks while the DMN is typically suppressed (3-6). Additionally, these activity changes are accompanied by concurrent increases in SN intra-network connectivity and decreased connectivity between SN and DMN (2, 4, 7). These networks have since been implicated in a wide range of cognitive tasks (3, 8). Specifically, the SN is a paralimbic-limbic network which plays a crucial role in identifying the most salient external events for adaptively guiding attention and behavior and for integrating cognitive, homeostatic, motivational, and affective signals (2, 7). In contrast, the DMN is a large-scale network anchored in cortical midline structures which is essential for internally oriented cognitive processes such as daydreaming, memory retrieval, future planning, and for integrating social information (9). Dysfunctional interactions between the SN and DMN are prominent in a wide range of psychiatric and neurological disorders including autism, attention deficit hyperactivity disorder, substance use disorder, depression, schizophrenia, and obsessive compulsive disorder (8, 10-12). Consequently, characterization of the neural mechanisms underlying DMN-SN interactions has significant clinical and translational relevance.

Non-invasive *in* vivo fMRI has played an important role in our understanding of the macroscopic functional organization of the SN and DMN. Computational analyses of causal dynamics in human fMRI data has suggested that the anterior insular cortex (AI), a key node of the SN, exerts the strongest inhibitory causal outflow to the DMN (4). However, whether the AI directly suppresses the DMN, and influences dynamic interactions between the SN and DMN has not been empirically validated *in vivo* due to inherent constraints of human imaging, such as the unavailability of tools for selectively manipulating neuronal activity and network interactions. Furthermore, a lack of integration across scales and model systems has severely limited our understanding of how mesoscale neural processes influence macroscopic functional brain networks. Thus, to address these critical knowledge gaps, we use animal models and take advantage of invasive optogenetic tools, which provide versatile control of brain-circuit function by selective manipulations (13-15).

Causal manipulation of brain circuits with simultaneous whole-brain recordings has the potential to advance our understanding of the functional organization of large-scale brain networks in ways that resting-state fMRI alone cannot. Notably, a number of contradictory and inconsistent findings have been reported in the literature with respect to the intrinsic functional organization of the rodent SN and DMN (16-28). While analysis of functional connectivity using resting-state fMRI has identified a rodent DMN anchored in the retrosplenial cortex (RSC) (17, 23), analogous to the human posterior cingulate cortex and extended posterior medial cortex, there is less agreement about inclusion of medial prefrontal cortex (mPFC) DMN nodes, such as the cingulate cortex (Cg) and prelimbic cortex (PrL) (20, 22-24, 26, 27). Indeed, in a recent study characterizing the rodent SN, Cg and PrL were implicated as nodes of the SN in addition to their putative roles in the DMN (17). Recent imaging studies have also paradoxically assigned individual subdivisions of the RSC and medial prefrontal cortex to both the SN and DMN (17, 29-32). Furthermore, the RSC is one of the largest cortical regions in rodents, and there is

growing evidence for functional heterogeneity along its anterior/posterior (A/P) axis (16). It follows that to accurately identify and model DMN-SN functional interactions, it is necessary to directly probe the functional involvement of Cg, PrL, as well as multiple RSC subdivisions in these networks. An important step in that direction is to probe circuit dynamics directly by selective manipulation of individual brain regions.

Here we leverage optogenetic-fMRI technology (13, 14, 28, 33-42) and recent advances in computational modeling of brain-circuit dynamics (43) to characterize the causal role of the AI in dynamic functional interactions between putative nodes of the rat SN and DMN including the AI, Cg, PrL, and multiple subdivisions of the RSC. We selectively applied feedforward optogenetic stimulation to Chronos-expressing neurons in the AI of experimental rats (hereafter referred to as Chronos rats) and enhanced yellow fluorescent protein-expressing neurons in the AI of control rats (EYFP rats) (**Figure 1A**). We then used a Bayesian Switching Dynamic Systems (BSDS) state-space algorithm (43) to determine stimulation-induced changes in dynamic functional brain circuits associated with the SN and DMN (**Figure 2A**). BSDS implements a hidden Markov model and unsupervised learning algorithm for determining latent brain states and dynamic switching processes from observed time-series data (43). BSDS belongs to a class of latent space switching models (44, 45) which go beyond traditional methods for recovering the structure of non-stationary time-varying organization of neural circuits (43, 46, 47). Notably, BSDS does not require arbitrary sliding windows nor does it impose temporal boundaries associated with predefined task conditions (43). BSDS applies a hidden Markov model to latent dynamic processes resulting in a parsimonious model of generators underlying the observed data, which is in contrast to approaches that apply a hidden Markov model directly to the observed fMRI data (48) (See also *Supplementary Information: Methods*). We used BSDS to evaluate the temporal dynamic properties of brain states, including probability of occurrence of individual brain states, state transition probabilities, as well as time-varying activation and functional connectivity induced by AI stimulation (**Figure 2B**).

We hypothesized that feedforward optogenetic stimulation of the AI would produce detectable brain states corresponding to periods with and without AI stimulation, each with a distinct pattern of activity and functional connectivity among putative SN and DMN nodes (**Figure 2C**). We further predicted that AI stimulation would result in suppression of RSC activity (deactivation), decreased connectivity of the AI with the RSC, together with enhanced Cg and PrL activity and connectivity indicative of their differential roles in SN and DMN function and network dynamics. Based on prior findings of latent brain state dynamics during human cognition (43), we hypothesized that a state-space model-based approach would uncover dynamic brain circuits associated with SN and DMN interactions, including transient states which occurred between periods on and off AI stimulation. This allowed us to uncover brain state dynamics which were not time-locked to experimental task conditions and not detectable by conventional analyses.

Our findings demonstrate that feedforward optogenetic AI stimulation induces dynamic suppression and decoupling of specific RSC subdivisions of the DMN, clarify causal mechanisms underlying dynamic cross-network interactions between the SN and DMN, and advance our understanding of rodent brain network organization.

Results

Optogenetic stimulation of AI and analysis of brain state dynamics

We applied feedforward optogenetic stimulation in an eight-epoch design to the right AI of nine Chronos rats and seven EYFP rats during cerebral blood volume (CBV) contrast-enhanced fMRI and extracted time-series data from nine regions of interest (ROIs) in the brain (**Figure 1A** and **Figure S1 and S2).** In each rat, the success of Chronos or EYFP viral vector expression was confirmed by histology (**Figure 1B**), and optical fiber placement was determined to be within the right AI by high-resolution anatomical T2-weighted MR images and individual locations were transcribed onto the Paxinos and Watson rat brain atlas, 6th edition (49) (**Figure 1C**), validating our manipulation locations. We confirmed the AI response to stimulation in the raw time-series data extracted from the AI ROI in ChR2 rats (**Figure 1D**), and did not observe any qualitative changes to stimulation in the AI signal from EYFP controls (**Figure 1E**).

We used BSDS to investigate dynamic changes in SN-DMN interactions associated with canonical nodes of the SN and DMN. We chose anatomically-defined SN and DMN nodes in the AI, PrL, Cg, and RSC based on a wide range of published studies (16, 17, 20, 22-27) (**Figure 1F** and **Table 1;** see also *Supplementary Information: Discussion*). Notably, these regions have been the focus of investigations of the functional organization of the rodent SN and DMN. Based on prior reports of functional heterogeneity within the RSC (16, 25, 50), we divided this node into six subdivisions, spaced in 1 mm intervals along the anterior-to-posterior axis, allowing us to determine which subdivisions were most strongly coupled or decoupled with the AI during stimulation. Additionally, this facilitated identification of heterogeneous responses and connectivity along the AP axis of the RSC. BSDS was applied to ROI time-series data to identify brain states and determine their spatiotemporal properties associated with AI stimulation, including time-varying posterior probabilities and occupancy rates of each state, and transition probabilities between states (**Figure 2A, B**). Finally, we examined the pattern of activation and functional connectivity among ROIs corresponding to each stimulation-related brain state in order to investigate dynamic functional interactions between putative nodes of the rat SN and DMN **(Figure 2C**). Notably, BSDS allowed us to capture dynamic circuit properties that are missed by conventional approaches (see **Figure S1** and *Supplementary Information: Discussion* for details).

Differentiation of brain states associated with optogenetic stimulation of AI in Chronos versus EYFP rats

Optogenetic stimulation of the AI in Chronos rats induced five distinct latent brain states defined by their unique spatiotemporal properties. In each rat, BSDS estimated the posterior probability of each latent brain state at each time point (**Figure 3A, top**), and the latent brain state with the highest posterior probability was chosen as the dominant state at that point for that subject (**Figure 3A, bottom**). Each latent brain state showed distinct moment-by-moment changes in posterior probability across time blocks with stimulation, and without stimulation, hereafter referred to as stimulation ON blocks and stimulation OFF blocks, respectively (**Figure 3A**). In contrast, while three distinct latent brain states were detected in EYFP rats, these did not show stimulation-dependent changes in posterior probability (**Figure 3B**).

To further determine whether latent brain-state dynamics differentiate AI stimulation conditions, we conducted multivariate classification analyses using a Linear Support Vector Machine (LSVM) algorithm and leave-one-out cross-validation (LOOCV) (see *Supplementary Information: Materials and Methods* for details). Classification models trained on posterior probabilities of latent brain states in Chronos rats accurately predicted stimulation ON blocks on unseen data with 74.7% accuracy, which significantly exceeds the chance level of 50% (p = 0.002, permutation test) (**Figure 3C**). The classification analyses using the same approach on the posterior probabilities of latent brain states in the EYFP rats showed only a chance-level classification accuracy of 50% (**Figure 3C**). These results demonstrate that the posterior probabilities of latent brain states distinguish stimulation ON from stimulation OFF blocks in Chronos, but not EYFP rats, thus providing evidence for specificity of brain states induced by AI stimulation.

Temporal properties of latent brain states corresponding to stimulation ON and stimulation OFF blocks

We next examined occupancy rates of latent brain states during the stimulation ON and OFF blocks. Occupancy rate quantifies the fraction of time a given state is most likely to occur. Examination of AI stimulation effects on the temporal properties of each state revealed that State 1 has a significantly higher occupancy rate than other states during stimulation OFF blocks (all *ps* < 0.05, two-tailed *t*-test, FDR-corrected, **Figure 3D**). Furthermore, the occupancy rate of State 1 was significantly higher during stimulation OFF compared to stimulation ON blocks ($p < 0.05$, two-tailed *t*-test, FDR-corrected, **Figure 3D**), suggesting that State 1 is the dominant state associated with the stimulation OFF blocks (hence, the OFF state). In contrast, State 2 had a significantly higher occupancy rate than other states during stimulation ON blocks (all *ps* < 0.05, two-tailed *t*-test, FDR-corrected, **Figure 3D**). Furthermore, the occupancy rate of State 2 was significantly higher during stimulation ON compared to stimulation OFF blocks ($p < 0.05$, two-tailed *t*-test, FDR-corrected, **Figure 3D**), implying that State 2 is a dominant state associated with the stimulation ON blocks (hence, the ON state). In EYFP rats, a single state (i.e., State 1) dominated both stimulation ON and OFF blocks (all *ps* < 0.05, two-tailed *t*-test, FDR-corrected, **Figure 3E**). Additional analyses using 10 s sub-blocks from the stimulation paradigm confirmed the predominance of States 1 and 2 across stimulation ON and OFF blocks, respectively (**Figure S3**, see *Supplementary Information: Results for further details*). Additional analyses revealed that the latent ON and OFF states have a mutually inhibitory influence on each other (**Figure S4,** see *Supplemental Information: Results* for further details). Taken together, these results demonstrate that stimulation ON and OFF blocks are dominated by distinct latent brain states in Chronos rats, but not in EYFP rats (**Figure 3F**).

Differences in regional activation between the ON and OFF brain states

We examined the effects of AI stimulation on activation and deactivation of each ROI during the ON and OFF brain states estimated by BSDS (**Figure 4A, B,** see *Supplementary Information: Materials and Methods* for details). BSDS model-based analysis identified strong evoked responses in the AI in Chronos rats (**Figure 4A**). Notably, AI stimulation in Chronos rats

resulted in suppression of multiple sections of the RSC spanning its anterior-to-middle subdivisions from –2.90 to -5.90 mm AP (**Figure 4A, B**, all *ps* < 0.05, two-tailed *t*-test, FDR corrected). In addition, this analysis revealed significant activation of the AI, PrL, and a posterior node of RSC at –6.86 mm AP (**Figure 4A, B**, all *ps* < 0.05, two-tailed *t*-test, FDR corrected), but no change in Cg activity. These results demonstrate the causal influence of AI stimulation on suppression of the DMN, identify the RSC area from –2.90 to –5.90 mm AP as a critical DMN node, and point to the involvement of the AI and PrL in the SN.

Differences in regional functional connectivity between the ON and OFF brain states

We then examined changes in dynamic functional connectivity associated with the ON and OFF brain states derived by the BSDS model in Chronos rats. Univariate link-specific analysis was conducted to determine unique functional connectivity patterns that differentiate the ON and OFF states (see *Supplementary Information: Materials and Methods* for details). This analysis revealed that the ON state has unique connectivity patterns compared to the OFF state (all *ps* < 0.05, two-tailed *t*-test, FDR corrected). Notably, the ON state showed decreased connectivity between AI and an anterior RSC region (-2.90 mm AP), suggesting decoupling between SN and DMN (**Figure 4C** and **4D**). In addition, the ON state also showed increased connectivity between the PrL and Cg, and the PrL and a middle RSC subdivision (-5.90 mm AP; **Figure 4C** and **4E**), but decreased connectivity between the PrL and posterior RSC (-7.82 mm AP; Figure **4C** and **4E**) and between anterior and posterior RSC subdivisions (**Figure 4C** and **4F**). Direct estimation of functional connectivity using data from time-points corresponding to the BSDS-derived ON and OFF states yielded convergent results and validated our findings (**Figure S5 and S6**; see *Supplementary Information: Results* for details). Collectively, these results suggest functional involvement of the PrL and Cg and functional heterogeneity within the RSC underlying SN-DMN dynamics.

Transient latent brain states induced by optogenetic stimulation in Chronos rats

BSDS also uncovered a third state (State 3, **Figure 3D**) in Chronos rats. We used BSDS-derived state switching probabilities to investigate the functional role of this state at the boundary between the OFF and ON stimulation blocks (i.e., the Transition state, see **Figure S7** and *Supplementary Information: Results* for details). Our analysis revealed that, at the OFF→ON stimulation boundary, the switching probabilities from the OFF to Transition state (i.e., $P_{OFF \rightarrow Transition}$) and from Transition to ON state (i.e., $P_{Transition \rightarrow ON}$) were both significantly higher than the switching probabilities from the OFF to ON state (i.e., $P_{OFF \rightarrow ON}$) (all *ps* < 0.001, two-tailed *t*-test, FDR-corrected, **Figure 5A**). Similarly, at the ON→OFF stimulation boundary, the switching probabilities from the ON state to Transition state (i.e., $P_{ON \rightarrow Transition}$) and from the Transition state to OFF state (i.e., $P_{Transition \rightarrow OFF}$) were both significantly higher than the switching probability from the ON to OFF state (i.e., $P_{ON \rightarrow OFF}$) (all *ps* < 0.001, two-tailed *t*-test, FDR-corrected, **Figure 5A**). Further analysis of counting switching paths between the OFF and ON states at the stimulation boundaries in each rat revealed that these states first pass through the Transition State rather than switching directly (all *ps* < 0.001, two-tailed *t*-test, **Figure 5B**). Two other states (States 4 and 5) had low occurrence (**Figure 3D**), and did not function as transition states between the OFF and ON states. Together, these results demonstrate that switching between OFF to ON states occurs via a robust Transition state (**Figure 5C**).

Comparison of activation and functional connectivity during the Transition state compared to the OFF state

Leveraging the power of latent brain models, we sought to determine changes in putative rat DMN and SN node activation and functional connectivity between the OFF and Transition brain states, as this is an intermediate step in the dynamic transition from the OFF to the ON state. Notably, in comparison to the OFF state, the Transition state following AI stimulation in Chronos rats showed suppression of multiple subdivisions of the RSC spanning its anterior to mid-regions (–2.90 to –4.86 mm AP), but activation of posterior subdivisions (-6.86 and –7.82mm AP) (**Figure 6A, B,** all *ps* < 0.05, two-tailed *t*-test, FDR corrected). Further, while the AI was also activated *(p* < 0.05, two-tailed *t*-test, FDR corrected), Cg and PrL did not exhibit significant activity changes during the Transition state **(Figure 6A, B)**.

We next examined differences in functional connectivity between the Transition and OFF states. Our analysis revealed that, compared to the OFF state, the Transition state was characterized by stronger functional connectivity between the AI and a mid-region of the RSC (-5.90 mm AP), but reduced intra-RSC connectivity between anterior (-2.90 and –3.86 mm AP) and mid-posterior subdivisions of RSC (-5.90 and -6.86 mm AP) (**Figure 6C,** all *ps* < 0.05, two-tailed *t*-test, FDR corrected). There were no significant differences involving Cg and PrL nodes. Taken together, these results demonstrate that AI stimulation in rats results in transient brain states characterized by heterogenous profiles of deactivation, activation and connectivity along the anterior-posterior axis of the RSC.

Comparison of activation and functional connectivity during the ON state compared to the Transition state

We then sought to determine how regional activation levels associated with AI-stimulation change from the Transition state to the ON state. Our analysis revealed significant increases in AI, PrL, and Cg activation during the ON state, compared to Transition state. In contrast, the posterior subdivisions of RSC (-5.90 mm and -6.86 mm AP) were suppressed during the ON compared to the Transition state (**Figure 6D, E**, all *ps* < 0.05, two-tailed *t*-test, FDR-corrected). Analysis of differences in regional functional connectivity between the ON and Transition states revealed decreased connectivity in the ON state between the AI and an anterior RSC subdivision (-2.90 mm AP), suggesting decoupling between SN and DMN. In addition, the ON state also showed increased connectivity between the PrL and Cg, but decreased connectivity between the anterior-middle RSC subdivisions (-3.86 mm, -4.86 mm AP) and posterior RSC (-6.86 mm, -7.82 mm AP) subdivisions (**Figure 6F**, all *ps* < 0.05, two-tailed *t*-test, FDR-corrected). Overall, the results from comparison of the ON state to the Transition state are in agreement with those from comparison of the ON state to the OFF state. Direct estimation of functional connectivity using data from time-points corresponding to the BSDS-derived Transition, ON and OFF states yielded convergent results and validated our findings (**Figure S8**). Collectively, these results provide further evidence for the functional involvement of the PrL and Cg nodes in SN-DMN dynamics, and suppression of RSC nodes of the DMN as well as functional heterogeneity within the RSC underlying SN-DMN interactions.

Replication of findings using extended SN and DMN ROIs

To determine the robustness of our findings with respect to ROI selection, we conducted additional analyses by incorporating amygdala and hippocampus nodes, which are known to be part of SN (17) and DMN (23), respectively (**Figure S9**). All major findings were replicated with this more general resting-state network-derived choice of ROIs (see *Supplemental Information: Results* for details). All major findings were also replicated when striatal and medial temporal lobe (MTL) ROIs, uncovered by conventional general linear model analysis (**Figure S1**), were included with the original SN and DMN nodes (**Figure S10**). These findings suggest that the putative SN and DMN nodes originally selected to test our *a priori* hypotheses are representative of these networks, and provide replicable information to capture the latent brain states underlying dynamic SN-DMN interactions induced by optogenetic stimulation of the AI.

Control analyses using ROIs located outside the SN and DMN

To further investigate the specificity of our findings with respect to ROI selection, we used BSDS to identify brain states from nodes in the auditory, visual, and motor cortex (**Figure S11**). We found that none of the main findings reported above were observed with the latent brain states estimates from this analysis (see *Supplementary Information: Results* for details). Taken together, these results demonstrate the specificity of our findings with respect to canonical SN-DMN ROIs.

Discussion

We combined selective feedforward optogenetic manipulation with simultaneous fMRI to determine the causal role of the AI in a potentially antagonistic relationship between the SN and DMN in the rat brain. Our computational approach using state-space modeling revealed five key findings associated with AI feedforward stimulation: (1) Distinct stable brain states of patterned activity corresponding to periods with and without AI stimulation; (2) DMN suppression of specific subdivisions of the RSC; (3) Activation of the AI and PrL; (4) Decreased AI connectivity with RSC, increased PrL and Cg connectivity, and decreased connectivity between RSC subdivisions; and (5) A transition state corresponding to the periods between stimulation conditions, characterized by a heterogenous profile of RSC suppression and activation, as well as increased AI to RSC and decreased intra-RSC connectivity. These findings were specific to stimulation of Chronos-expressing neurons in experimental rats and were not observed in EYFP-expressing control rats.

Our study demonstrates that AI stimulation induces dynamic suppression of the DMN and decoupling of the DMN from the SN. In addition, PrL activation and enhanced PrL-Cg coupling during AI stimulation indicates that these regions, commonly included in the rodent DMN, also have a functional role in the SN (17). Furthermore, AI stimulation-induced heterogenous deactivation and connectivity patterns along the AP axis of RSC, which were particularly apparent during the brief transition state, point to the existence of distinct functional modules within the rodent RSC. Our findings reveal circuit mechanisms underlying suppression of the DMN and demonstrate a causal role for the AI in network switching. Findings also identify

several dynamical aspects of the functional organization of the SN and DMN in the rat brain and help clarify conflicting findings in the literature.

AI stimulation of Chronos-expressing neurons in experimental rats, but not EYFP controls, induced robust ON and OFF brain states characterized by distinct patterns of activity and connectivity between the AI, PrL Cg, and multiple nodes spanning the anterior-posterior axis of the RSC. Comparison of these states revealed that AI stimulation suppressed neuronal responses in the RSC, and reductions were observed in multiple subdivisions of the RSC spanning its anterior-posterior axis (**Figure 4**).

Importantly, our analyses also revealed heterogeneous activity changes in response to AI stimulation with a prominent role for the anterior to middle, but not posterior, aspects of the RSC in the rat DMN (**Figure 4A, B**). Convergent with our findings at the anterior RSC, Ferrier et al recently used single-slice functional ultrasound imaging in the mouse brain and reported that somatosensory sensory stimulation induces cerebral blood volume suppression in the anterior RSC (51). Our results also parallel findings from Fakhraei et al. who measured local field potentials in multiple rat brain areas and found suppression of anterior RSC during a behavioral inhibition task (50). Interestingly, suppression of the anterior RSC was linked with improved task performance, similar to findings previously reported in humans (52). Our results showing higher activation levels of anterior RSC in the OFF state than the ON state are in agreement with these studies, and highlight the role of RSC activation and deactivation in maintenance and suppression of the DMN. Crucially, these findings advance our knowledge by revealing a casual mechanism specifically tied to direct feedforward stimulation of AI neurons.

AI stimulation also decreased functional connectivity between the AI and anterior RSC (**Figure 4C**) as well as decoupling of the anterior from posterior RSC (**Figure 4C)**, demonstrating a causal mechanism underlying decoupling of the SN and DMN networks. Taken together, these results identify AI-induced focal suppression of RSC connectivity in rats which is consistent with observations of task-related decoupling of the SN and DMN in the human brain (2, 4, 7). This finding represents a critical step towards the use of rodent models for understanding the circuit mechanisms of dynamic network switching processes observed in the human brain (2, 8).

Direct stimulation of the AI provides clarification of circuit dynamics beyond resting-state fMRI, much like task-based activation studies and causal network analysis have provided in the context of human fMRI studies (8). Pertinent here is the question of the functional organization and distinctness of SN and DMN in the rodent brain, especially with respect to the PrL and Cg in the medial prefrontal cortex which have been variously assigned to both networks (17, 32). No clear distinctions from the viewpoint of intrinsic functional network-level organization have emerged, and maps based on independent component analyses have emphasized SN and DMN overlap in both the PrL and Cg (23). Indeed, while early studies of the DMN have suggested that the PrL and Cg might constitute its anterior node (17, 20, 32), anatomical tracer studies have pointed to direct pathways linking the PrL and Cg with the AI (17, 53) a pattern supporting our findings here. Further evidence supporting the involvement of these regions in the SN was recently described by Tsai et al., showing increased AI-Cg functional connectivity during naloxone cue-induced conditioned heroin withdrawal (17).

In this context, it is noteworthy that AI stimulation selectively suppressed activity and connectivity with the RSC, but not the PrL or Cg. Instead, in parallel with decreases in AI connectivity with the RSC, the PrL showed increased connectivity with Cg and decreased connectivity with the posterior RSC. Thus, stimulation related patterns suggest a state-specific alignment of the PrL and Cg more consistent with the SN, rather than the DMN. This finding should not be surprising as the PrL and Cg have been implicated in frontal control of memory, attention and reward processing in the rodent brain (54). The PrL has also been implicated in processing information from the environment, including drug cues (55, 56). Consistent with this view, a recent study using whole brain fMRI in rats found that novelty preferences and cocaine-associated cues influence PrL association with the SN (57). It is also possible that the functional distinctions of these medial frontal regions are not as well aligned into an SN-DMN dichotomy as observed in the human brain, consistent with reports of divergent rodent and primate medial frontal cortex functional connectivity(58). Indeed, while chemogenetic suppression of Cg has been shown to reduce RSC activity and overall DMN connectivity (27, 59), a recent study by Tu et al. showed that such manipulation also increases the centrality of RSC and promotes the emergence of the RSC hub of DMN (60). Consistent with our findings, these results may suggest that Cg and PrL are involved in both SN and DMN, and these networks might be less segregated in rodents than in primates. Further research with manipulations of PrL and Cg with whole brain fMRI is required to clarify circuit mechanisms of network organization and function across species.

An important question raised by our findings is whether AI stimulation induces DMN suppression via direct or indirect pathways. Our observation that AI stimulation modulates RSC activity and connectivity in the rat is intriguing given the lack of evidence for direct anatomical connections between the two structures in rodents (61-64). Although it is tempting to assume that functional connectivity implies direct anatomical connectivity, it has long been established that the relationship between the two is far more complex; as such, even sparse indirect connections can be sufficient to induce changes in functional connectivity (65, 66). We suggest that information flow between AI and RSC may rely on one or more intermediary nodes in the mPFC. Indeed, rodent tract-tracing studies reveal that the AI is connected to Cg and PrL (17, 19, 63, 67), which in turn are connected to the RSC via the cingulum bundle (63). The PrL is also directly connected to Cg, and given that RSC has relatively dense connectivity with Cg compared to other prefrontal regions, a multi-node pathway for information flow from AI→PrL→Cg→RSC is also plausible. In addition, the claustrum may be an alternative intermediary node for AI-RSC connectivity, as it is bidirectionally connected with AI, prefrontal regions, and RSC (63), and recent evidence supports a role for this structure in SN-DMN interactions (68, 69). Characterizing the functional and causal role of these putative information flow pathways in SN-DMN dynamics is an important goal for future studies. Because the temporal resolution of fMRI limits inferences about directionality of communication via intermediary nodes, electrophysiological studies may be required to delineate multi-node pathways.

Our computational analysis also revealed a short-lived, but stable, state that occurred during the transition between the OFF and ON states. Analysis of this state, which could not have been identified using conventional general linear models, revealed that transitions from the OFF to ON states likely occur by passing through this third, transition, state (**Figure 5**). No such state

was present in EYFP rats. Thus, our computational methods not only uncovered AI stimulation-induced brain states, but also transition states and their temporal boundaries. A particularly powerful feature of our modeling approach is therefore the ability to capture transition states which can carry information about short-lived changes that can be missed by conventional approaches. This allowed us to uncover several important facets of SN-DMN circuit dynamics.

Further analysis of the transition state revealed four features of activation and connectivity changes in the RSC associated with AI stimulation (**Figure 6**). First, the transition state was characterized by strong suppression of anterior to middle RSC subdivisions in Chronos rats, with levels higher than those seen between OFF and ON states. Thus, this state captures a large change in fMRI response properties that occur during the transition from the OFF to ON states. Second, there was a transient increase in posterior RSC activity with AI stimulation. Third, during the transition state, AI connectivity with a specific middle RSC subdivision increased above levels observed in the OFF state. Fourth, the transition state was characterized by decreased connectivity between anterior and middle RSC subdivisions. Collectively, these results demonstrate that dynamic state changes induced by AI stimulation in the rat brain begin with a heterogenous pattern of node-specific transient suppression along the AP axis of the RSC, in parallel with short-lived subregion-specific AI-RSC coupling and intra-RSC decoupling. These findings further reveal heterogenous profiles of changes in functional circuits and hint at inhibitory processes that may serve to transiently create distinct functional boundaries within the RSC such as those observed during various stages of memory formation in the rodent brain (16).

The RSC is involved in a variety of cognitive tasks including memory, navigation, and prospective thinking, yet the precise role of the rodent RSC and the functional differences between its subdivisions remain elusive (25). Our analyses revealed AI-stimulation-induced heterogeneity within RSC consistent with recent reports about its functional organization along the anterior-posterior axis (16). While rodent resting-state fMRI studies have treated the RSC as a homogeneous region, electrophysiological and optogenetic studies suggest that the RSC contains multiple cytoarchitectonic divisions (16, 25). Consistent with our findings, optogenetic inhibition of neuronal activity in the anterior and posterior RSC revealed divergent impacts on behavior evoked by conditioned stimuli (16). Taken together, these findings suggest that the RSC comprises distinct functional modules, consistent with our finding of clear differences in connectivity patterns associated with stimulation of AI. Further studies with behaviorally relevant salient stimuli in awake rodents, whole-brain imaging, and causal circuit manipulations, including inhibition of the AI, mPFC nodes and RSC, will advance our understanding of RSC functional heterogeneity. It is noteworthy here that heterogeneity along the anterior/posterior axis of the posterior cingulate cortex is also a prominent feature of the human DMN (70), and optogenetic manipulations with whole-brain imaging have the potential to inform the underlying causal circuit mechanisms.

In summary, our study demonstrates that feedforward optogenetic stimulation of the AI suppresses activation of the DMN and dynamically decouples SN and DMN. These findings parallel reports of decreased connectivity between SN and DMN observed during working memory and other cognitively demanding tasks in humans (2, 4, 7). Notably, direct stimulation of neurons allowed us to address limitations of prior noninvasive studies and probe the direct effects of manipulation of neuronal activity in the AI. Our study elucidates causal mechanisms

underlying neuronal perturbation of cross-network interactions involving the SN and DMN and converges on previous reports in human fMRI studies implicating the AI in network switching (8). Our findings also suggest that PrL and Cg, commonly included in the rodent DMN, may also have a functional role in the SN, pointing to lower levels of network segregation in rodents than in primates. More generally, our dynamical systems approach and findings address critical gaps in our understanding of the cellular organization of brain networks (71, 72) and provide a translational model for investigating aberrant network switching in psychiatric disorders (73, 74). Finally, our innovative computational tools and analytic approach will be useful for investigations of latent processes underlying brain function and dysfunction.

Materials and Methods

Data Acquisition

Surgical preparation of rats for optogenetic manipulation: Sixteen Male Sprague Dawley rats weighing ~300 g at time of surgical preparation were separated into experimental (Chronos, n = 9) and control (EYFP, n = 7) groups for these studies. During stereotactic surgery, rats were isoflurane anesthetized (4% induction, 2% maintenance) and all procedures conducted using sterile techniques. After exposing the skull, a craniotomy was drilled above the right AI and a 30 G infusion cannula preloaded with virus was slowly lowered into the right AI at the following coordinate from skull at Bregma according to the Paxinos and Watson rat brain atlas, 6th edition: 2.75 mm AP, 3.75 mm medial-lateral, –6.00 mm dorsal-ventral. After allowing the brain tissue to settle, the cannula was raised 0.1 mm and 1 ul of AAV5-hSyn-Chronos at a flow rate of 0.1 was infused at a flow rate of 0.1 ul/min into the right AI of Chronos rats. Following the virus infusion, ten minutes were given to allow virus diffusion before the infusion cannula was retracted.

Chronos was chosen for selective feedforward control of AI neurons because of its superior spiking fidelity (75) and efficiency in recruiting axonal feedforward activity during repetitive stimulation compared to conventional channelrhodopsin-2 (76). The pan-neuronal hSyn promoter was chosen for its high transduction efficiency in cortex (77), and because further neuronal specificity was not required as the AI sends exclusively excitatory projections to other brain regions (67). Control rats received the same preparation, but with a AAV5-hSyn-EYFP control vector to express only EYFP instead of Chronos. The required vectors were prepared and packaged with a titer of ~10^{12} vg/ml by the UNC Vector Core at UNC Chapel Hill.

During the same surgery, following virus infusion, an optical fiber (200 µm core, .22 NA) was implanted just above the infusion site at DV –5.70 mm to enable light delivery to the right AI for optogenetic stimulation. Thereafter, 3 or 4 MR-compatible brass screws were secured into the skull near the lateral ridges without damaging brain tissue. Dental cement was then spread over the exposed skull surface to firmly secure the optical fiber in place with MR-compatible brass screws serving as anchor points. Surgical implantation accuracy of optical fibers was verified with anatomical MRI scans (T_2-weighted RARE sequences) at the beginning of fMRI sessions (**Figure 1C**) (14, 78).

Following fMRI scanning, subjects were deeply anesthetized and transcardially perfused with saline, followed by 4% paraformaldehyde, to affix brain tissue for histological verification of viral vector expression. Brains were postfixed in 4% paraformaldehyde for 24 h and transferred to 30% sucrose for 48 h before sectioning into 40 µm coronal slices by cryostat. Sections spanning the AI were then mounted and coverslipped with Fluoroshield with DAPI (Sigma Aldrich). Finally, mounted brain sections were visualized using an Olympus MVX10 wide field scope with 5x objective to confirm virus expression in AI, and obtain representative images.

Preparation of rats for fMRI scanning: Approximately thirty-minutes prior to fMRI scanning, rats were anesthetized with 2% isoflurane in medical air (4% for induction), orotracheally intubated and mechanically ventilated, and outfitted with an intravenous tail-vein catheter. Next, rats were secured in a custom MRI cradle and a fiber optic patch cable (200 µm core, .22 NA, 7 m long), set to deliver blue light from a solid-state laser, was connected to the implanted fiber in each rat for optogenetic stimulation of the AI. Subsequently, rats were positioned in the MRI bore, anatomical scans were completed, then a functional scan was acquired during which the CBV contrast agent Feraheme (30 mg/kg intravenous) was administered to augment detection sensitivity and measure CBV-weighted signal changes (41, 79-81). Finally, rats were switched to a well-established sedation protocol combining low dose (0.5%) isoflurane with a cocktail of intravenous dexmedetomidine (0.05 mg/kg/hr) and pancuronium (0.5 mg/kg/hr), and allowed 30 minutes for their physiological parameters to stabilize before optogenetic-fMRI scanning. Importantly, this light sedation protocol has been shown to preserve neurovascular coupling for functional connectivity studies (82-87) . Throughout fMRI scanning procedures, animal physiology was continuously monitored and maintained within physiologically desirable limits, including a 3.0±0.3% end-tidal CO_2, 250-320 bpm heart rate, 93±5% oxygen saturation (SpO_2), and 37.5 ± 1 °C core temperature.

MRI acquisition protocols: fMRI studies were performed on a Bruker 9.4-Tesla/30-cm scanner with a BGA9-S gradient insert in the Center for Animal Magnetic Resonance Imaging at UNC Chapel Hill. A homemade surface coil (1.6 cm inner diameter), designed to not obstruct optical fibers, was used as the RF transceiver. Magnetic field homogeneity was optimized by global shim followed by local first- and second-order shims using the standard FASTMAP protocol (88). All MRI acquisitions were in anisotropic resolution with 12 coronal slices, 1 mm thick and 1 mm apart, aligned on the AP axis such that the fifth-most anterior slice was centered on the anterior commissure (corresponding to -0.36 mm AP) for each rat. fMRI scans were acquired with a single shot, gradient echo-EPI sequence optimized for the Feraheme CBV contrast agent with the following parameters: spectral width = 300 kHz, TR/TE = 1000/8 ms, FOV = 2.56 x 2.56 cm^2, matrix size = 80x80. Anatomical images were acquired using a T2-weighted RARE sequence with the following parameters: spectral width: 47 kHz, TR/TE = 2500/33 ms, FOV = 2.56 x 2.56 cm^2, matrix size = 256 x 256, RARE factor = 8, averages = 8. The initial Feraheme infusion fMRI scan was 300 s in duration and included a minimum of 60 s before and after the infusion to acquire the pre- and post-Feraheme image intensities, respectively. CBV contrast was confirmed for each rat by comparing pre- and post-Feraheme image intensities. Optogenetic-fMRI scans were acquired in a single 1160 s run for each animal, beginning with a stimulation OFF resting period for the initial 360 s followed by an 800 s period of repeated stimulation blocks described below.

Optogenetic stimulation: Stimulation was delivered in a repeated epoch design, consisting of 8 repetitions of a 20 s "ON" block of pulsed 473 nm blue-light delivery via the chronically-implanted optical fiber in AI followed by an 80 s "OFF" block without stimulation to allow recovery of neuronal activity to baseline. Based on the extant literature (41, 89), stimulation light pulses were delivered at 20 Hz (10 mW power at fiber tip, 5 ms pulse width).

Data Analysis

fMRI preprocessing: All MRI images were preprocessed using AFNI (http://afni.nimh.nih.gov/afni/). Briefly, a group template based on individual T2-weighted images was generated using procedures described by Kazemi et al (90). Individual subject fMRI data were then slice-timing corrected and realigned to the mean image to correct head-motion. Six degree of freedom motion parameters were estimated through the realignment step. Aligned images were then co-registered to the T2-weighted anatomical scan followed by spatially normalization to the T2-weighted group template using linear affine registration. The normalized functional images were resampled from 0.32 x 0.32 x 1 mm voxel size to 0.5 mm isotropic voxel size. Nuisance removal including detrending with 3rd order polynomial fitting, a high-pass filter with frequency cut at 0.01 Hz and regressing out the head motion parameters. Finally, a 1 mm FWHM Gaussian kernel was applied for spatial smoothing.

ROI time series: To test our hypotheses related to dynamic changes in the SN and DMN induced by optogenetic stimulation of the AI, and to avoid circularity arising from bias in selection (91), we used nine anatomically-defined canonical salience (SN) and default mode network (DMN) nodes encompassing the AI, PrL, Cg, and RSC (16, 17, 20-28). The precise locations of these nodes were based on a wide range of published studies in rodents (16, 17, 20-28). Because of its relatively large size, and growing evidence for functional heterogeneity of the RSC along its anterior/posterior axis (16), we demarcated six ROIs along the A/P axis of the RSC. Spherical ROIs 1 mm in diameter were placed at the center of mass within the anatomical boundaries of each region based on the Paxinos and Watson rat brain atlas, 6th edition (49), after co-registration to a group-template image space. **Table 1** shows the coordinates of each ROI used in the main analyses. Next, CBV-weighted time-series data were extracted from each ROI (noncontiguous bilateral ROIs were averaged) by inverting raw fMRI signal following intravenous administration of feraheme and displayed in percent raw signal changes (79). Finally, time courses were normalized for use in computational modeling and group comparisons. Control analyses were conducted using anatomically-defined ROIs in the (i) amygdala, hippocampus, (ii) striatum and MTL, and (iii) auditory, visual, and motor cortices (**Figure S9A**, **S10A, and S11A)**.

Bayesian Switching Dynamic Systems model: We used BSDS, based on a hidden Markov process model, to uncover latent brain states associated with optogenetic stimulation of AI. A detailed explanation of the model is in *Supplementary Information: Materials and Methods***.** Key measures extracted from BSDS include posterior probability, occupancy rate, and covariance of latent brain state.

Acknowledgements

This work was supported in part by National Institute of Mental Health (R01MH121069, R01MH126518, R01MH121069, RF1MH117053, R01MH111429), National Institute on Alcohol Abuse and Alcoholism (P60AA011605, U01AA020023, T32AA007573), National Institute of Neurological Disorders and Stroke (R01NS086085, R01NS091236), National Institute of Child Health and Human Development (P50HD103573), and National Institute of Biomedical Imaging and Bioengineering (R01EB022907). We thank members of the UNC Center for Animal MRI (CAMRI) for technical assistance and Drs. Harry Chao and Li-Ming Hsu for insightful discussions.

Competing interest

The authors declare no competing interests.

References

1. V. Menon, M. D'Esposito, The role of PFC networks in cognitive control and executive function. *Neuropsychopharmacology* **47**, 90-103 (2022).
2. V. Menon, L. Q. Uddin, Saliency, switching, attention and control: a network model of insula function. *Brain structure and function* **214**, 655-667 (2010).
3. W. W. Seeley *et al.*, Dissociable intrinsic connectivity networks for salience processing and executive control. *Journal of Neuroscience* **27**, 2349-2356 (2007).
4. W. Cai, S. Ryali, R. Pasumarthy, V. Talasila, V. Menon, Dynamic causal brain circuits during working memory and their functional controllability. *Nature Communications* **12**, 1-16 (2021).
5. M. D. Greicius, B. Krasnow, A. L. Reiss, V. Menon, Functional connectivity in the resting brain: a network analysis of the default mode hypothesis. *Proc Natl Acad Sci U S A* **100**, 253-258 (2003).
6. S. L. Bressler, V. Menon, Large-scale brain networks in cognition: emerging methods and principles. *Trends in cognitive sciences* **14**, 277-290 (2010).
7. V. Menon (2015) Salience Network: Brain Mapping: An Encyclopedic Reference. (Elsevier Inc).
8. D. Sridharan, D. J. Levitin, V. Menon, A critical role for the right fronto-insular cortex in switching between central-executive and default-mode networks. *Proceedings of the National Academy of Sciences* **105**, 12569-12574 (2008).
9. Y. Yeshurun, M. Nguyen, U. Hasson, The default mode network: where the idiosyncratic self meets the shared social world. *Nature Reviews Neuroscience* **22**, 181-192 (2021).
10. M. Goodkind *et al.*, Identification of a common neurobiological substrate for mental illness. *JAMA psychiatry* **72**, 305-315 (2015).
11. V. Menon, Large-scale brain networks and psychopathology: a unifying triple network model. *Trends in cognitive sciences* **15**, 483-506 (2011).
12. L. Q. Uddin *et al.*, Salience network–based classification and prediction of symptom severity in children with autism. *JAMA psychiatry* **70**, 869-879 (2013).
13. S. Ryali *et al.*, Combining optogenetic stimulation and fMRI to validate a multivariate dynamical systems model for estimating causal brain interactions. *Neuroimage* **132**, 398-405 (2016).
14. J. H. Lee *et al.*, Global and local fMRI signals driven by neurons defined optogenetically by type and wiring. *Nature* **465**, 788-792 (2010).
15. K. M. Tye, K. Deisseroth, Optogenetic investigation of neural circuits underlying brain disease in animal models. *Nature Reviews Neuroscience* **13**, 251-266 (2012).
16. S. Trask, S. E. Pullins, N. C. Ferrara, F. J. Helmstetter, The anterior retrosplenial cortex encodes event-related information and the posterior retrosplenial cortex encodes context-related information during memory formation. *Neuropsychopharmacology*, 1-7 (2021).
17. P.-J. Tsai *et al.*, Converging structural and functional evidence for a rat salience network. *Biological Psychiatry* **88**, 867-878 (2020).
18. A. S. Klein, N. Dolensek, C. Weiand, N. Gogolla, Fear balance is maintained by bodily feedback to the insular cortex in mice. *Science* **374**, 1010-1015 (2021).
19. H. Kayyal *et al.*, Insula to mPFC reciprocal connectivity differentially underlies novel taste neophobic response and learning in mice. *Elife* **10**, e66686 (2021).

20. J. M. Stafford *et al.*, Large-scale topology and the default mode network in the mouse connectome. *Proceedings of the National Academy of Sciences* **111**, 18745-18750 (2014).
21. M. Pagani *et al.*, mTOR-related synaptic pathology causes autism spectrum disorder-associated functional hyperconnectivity. *Nature communications* **12**, 1-15 (2021).
22. L. Coletta *et al.*, Network structure of the mouse brain connectome with voxel resolution. *Science Advances* **6**, eabb7187 (2020).
23. H. Lu *et al.*, Rat brains also have a default mode network. *Proc Natl Acad Sci U S A* **109**, 3979-3984 (2012).
24. J. D. Whitesell *et al.*, Regional, Layer, and Cell-Type-Specific Connectivity of the Mouse Default Mode Network. *Neuron* **109**, 545-559. e548 (2021).
25. J. Sugar, M. P. Witter, N. van Strien, N. Cappaert, The retrosplenial cortex: intrinsic connectivity and connections with the (para) hippocampal region in the rat. An interactive connectome. *Frontiers in neuroinformatics* **5**, 7 (2011).
26. J. Grandjean, V. Zerbi, J. H. Balsters, N. Wenderoth, M. Rudin, Structural basis of large-scale functional connectivity in the mouse. *Journal of Neuroscience* **37**, 8092-8101 (2017).
27. W. Tu, Z. Ma, Y. Ma, D. Dopfel, N. Zhang, Suppressing anterior cingulate cortex modulates default mode network and behavior in awake rats. *Cerebral cortex* **31**, 312-323 (2021).
28. F. Mandino *et al.*, A triple-network organization for the mouse brain. *Molecular Psychiatry*, 1-8 (2021).
29. J. T. Arsenault, N. Caspari, R. Vandenberghe, W. Vanduffel, Attention shifts recruit the monkey default mode network. *Journal of Neuroscience* **38**, 1202-1217 (2018).
30. L.-M. Hsu *et al.*, Constituents and functional implications of the rat default mode network. *Proceedings of the National Academy of Sciences* **113**, E4541-E4547 (2016).
31. D. Mantini *et al.*, Default mode of brain function in monkeys. *Journal of Neuroscience* **31**, 12954-12962 (2011).
32. A. Gozzi, A. J. Schwarz, Large-scale functional connectivity networks in the rodent brain. *Neuroimage* **127**, 496-509 (2016).
33. C. G. Cover *et al.*, Whole brain dynamics during optogenetic self-stimulation of the medial prefrontal cortex in mice. *Communications biology* **4**, 1-8 (2021).
34. W. Jing *et al.*, Reentrant information flow in electrophysiological rat default mode network. *Frontiers in neuroscience* **11**, 93 (2017).
35. E. A. Ferenczi *et al.*, Prefrontal cortical regulation of brainwide circuit dynamics and reward-related behavior. *Science* **351** (2016).
36. Y. Chen, P. Pais-Roldan, X. Chen, M. H. Frosz, X. Yu, MRI-guided robotic arm drives optogenetic fMRI with concurrent Ca 2+ recording. *Nature communications* **10**, 1-11 (2019).
37. Z. Liang *et al.*, Mapping the functional network of medial prefrontal cortex by combining optogenetics and fMRI in awake rats. *Neuroimage* **117**, 114-123 (2015).
38. M. Desai *et al.*, Mapping brain networks in awake mice using combined optical neural control and fMRI. *Journal of neurophysiology* **105**, 1393-1405 (2011).
39. A. T. Leong *et al.*, Long-range projections coordinate distributed brain-wide neural activity with a specific spatiotemporal profile. *Proceedings of the National Academy of Sciences* **113**, E8306-E8315 (2016).

40. F. Albers, L. Wachsmuth, D. Schache, H. Lambers, C. Faber, Functional mri readouts from bold and diffusion measurements differentially respond to optogenetic activation and tissue heating. *Frontiers in neuroscience* **13**, 1104 (2019).
41. H. K. Decot *et al.*, Coordination of brain-wide activity dynamics by dopaminergic neurons. *Neuropsychopharmacology* **42**, 615-627 (2017).
42. J. Grandjean *et al.*, A brain-wide functional map of the serotonergic responses to acute stress and fluoxetine. *Nature communications* **10**, 1-10 (2019).
43. J. Taghia *et al.*, Uncovering hidden brain state dynamics that regulate performance and decision-making during cognition. *Nature communications* **9**, 1-19 (2018).
44. J. Semedo, A. Zandvakili, A. Kohn, C. K. Machens, M. Y. Byron (2014) Extracting latent structure from multiple interacting neural populations. in *Advances in neural information processing systems*, pp 2942-2950.
45. J. I. Glaser, M. R. Whiteway, J. P. Cunningham, L. Paninski, S. W. Linderman, Recurrent switching dynamical systems models for multiple interacting neural populations. *bioRxiv* (2020).
46. B. Lee *et al.*, Latent brain state dynamics and cognitive flexibility in older adults. *Progress in Neurobiology*, 102180 (2021).
47. W. Cai *et al.*, Latent brain state dynamics distinguish behavioral variability, impaired decision-making, and inattention. *Molecular Psychiatry*, 1-14 (2021).
48. D. Vidaurre, S. M. Smith, M. W. Woolrich, Brain network dynamics are hierarchically organized in time. *Proceedings of the National Academy of Sciences* **114**, 12827-12832 (2017).
49. G. Paxinos, C. Watson, *The rat brain in stereotaxic coordinates: hard cover edition* (Elsevier, 2006).
50. L. Fakhraei *et al.*, Electrophysiological Correlates of Rodent Default-Mode Network Suppression Revealed by Large-Scale Local Field Potential Recordings. *Cerebral Cortex Communications* **2**, tgab034 (2021).
51. J. Ferrier, E. Tiran, T. Deffieux, M. Tanter, Z. Lenkei, Functional imaging evidence for task-induced deactivation and disconnection of a major default mode network hub in the mouse brain. *Proceedings of the National Academy of Sciences* **117**, 15270-15280 (2020).
52. A. Anticevic *et al.*, The role of default network deactivation in cognition and disease. *Trends in cognitive sciences* **16**, 584-592 (2012).
53. W. W. Seeley, The salience network: a neural system for perceiving and responding to homeostatic demands. *Journal of Neuroscience* **39**, 9878-9882 (2019).
54. P. Rajasethupathy *et al.*, Projections from neocortex mediate top-down control of memory retrieval. *Nature* **526**, 653-659 (2015).
55. W. Sun, G. V. Rebec, The role of prefrontal cortex D1-like and D2-like receptors in cocaine-seeking behavior in rats. *Psychopharmacology* **177**, 315-323 (2005).
56. A. R. Zavala, S. M. Weber, H. J. Rice, A. T. Alleweireldt, J. L. Neisewander, Role of the prelimbic subregion of the medial prefrontal cortex in acquisition, extinction, and reinstatement of cocaine-conditioned place preference. *Brain research* **990**, 157-164 (2003).
57. M. L. Rohan, S. B. Lowen, A. Rock, S. L. Andersen, Novelty preferences and cocaine-associated cues influence regions associated with the salience network in juvenile female rats. *Pharmacology Biochemistry and Behavior* **203**, 173117 (2021).

58. D. J. Schaeffer *et al.*, Divergence of rodent and primate medial frontal cortex functional connectivity. *Proceedings of the National Academy of Sciences* **117**, 21681-21689 (2020).
59. L. M. Peeters *et al.*, Chemogenetic silencing of neurons in the mouse anterior cingulate area modulates neuronal activity and functional connectivity. *Neuroimage* **220**, 117088 (2020).
60. W. Tu, Z. Ma, N. Zhang, Brain network reorganization after targeted attack at a hub region. *NeuroImage*, 118219 (2021).
61. L. L. Cloutman, R. J. Binney, M. Drakesmith, G. J. Parker, M. A. L. Ralph, The variation of function across the human insula mirrors its patterns of structural connectivity: evidence from in vivo probabilistic tractography. *Neuroimage* **59**, 3514-3521 (2012).
62. L. Cerliani *et al.*, Probabilistic tractography recovers a rostrocaudal trajectory of connectivity variability in the human insular cortex. *Human brain mapping* **33**, 2005-2034 (2012).
63. B. Zingg *et al.*, Neural networks of the mouse neocortex. *Cell* **156**, 1096-1111 (2014).
64. A. Jakab, P. P. Molnár, P. Bogner, M. Béres, E. L. Berényi, Connectivity-based parcellation reveals interhemispheric differences in the insula. *Brain topography* **25**, 264-271 (2012).
65. C. J. Honey *et al.*, Predicting human resting-state functional connectivity from structural connectivity. *Proceedings of the National Academy of Sciences* **106**, 2035-2040 (2009).
66. J. X. O'Reilly *et al.*, Causal effect of disconnection lesions on interhemispheric functional connectivity in rhesus monkeys. *Proceedings of the National Academy of Sciences* **110**, 13982-13987 (2013).
67. D. A. Gehrlach *et al.*, A whole-brain connectivity map of mouse insular cortex. *Elife* **9**, e55585 (2020).
68. Z. Chia, G. J. Augustine, G. Silberberg, Synaptic connectivity between the cortex and claustrum is organized into functional modules. *Current Biology* **30**, 2777-2790. e2774 (2020).
69. J. B. Smith *et al.*, A role for the claustrum in salience processing? *Frontiers in neuroanatomy* **13**, 64 (2019).
70. R. Leech, S. Kamourieh, C. F. Beckmann, D. J. Sharp, Fractionating the default mode network: distinct contributions of the ventral and dorsal posterior cingulate cortex to cognitive control. *Journal of Neuroscience* **31**, 3217-3224 (2011).
71. A. Devor *et al.*, The challenge of connecting the dots in the BRAIN. *Neuron* **80**, 270-274 (2013).
72. D. Badre, M. J. Frank, C. I. Moore, Interactionist neuroscience. *Neuron* **88**, 855-860 (2015).
73. V. Menon, Large-scale brain networks and psychopathology: a unifying triple network model. *Trends Cogn Sci* **15**, 483-506 (2011).
74. K. Supekar, W. Cai, R. Krishnadas, L. Palaniyappan, V. Menon, Dysregulated Brain Dynamics in a Triple-Network Saliency Model of Schizophrenia and Its Relation to Psychosis. *Biological psychiatry* **85**, 60-69 (2019).
75. N. C. Klapoetke *et al.*, Independent optical excitation of distinct neural populations. *Nature methods* **11**, 338-346 (2014).
76. C. A. Hass, L. L. Glickfeld, High-fidelity optical excitation of cortico-cortical projections at physiological frequencies. *Journal of neurophysiology* **116**, 2056-2066 (2016).

77. B. Nieuwenhuis *et al.*, Optimization of adeno-associated viral vector-mediated transduction of the corticospinal tract: comparison of four promoters. *Gene therapy* **28**, 56-74 (2021).
78. H.-Y. Lai, J. R. Younce, D. L. Albaugh, Y.-C. J. Kao, Y.-Y. I. Shih, Functional MRI reveals frequency-dependent responses during deep brain stimulation at the subthalamic nucleus or internal globus pallidus. *Neuroimage* **84**, 11-18 (2014).
79. S. G. Kim *et al.*, Cerebral blood volume MRI with intravascular superparamagnetic iron oxide nanoparticles. *NMR in Biomedicine* **26**, 949-962 (2013).
80. J. B. Mandeville *et al.*, Dynamic functional imaging of relative cerebral blood volume during rat forepaw stimulation. *Magnetic resonance in medicine* **39**, 615-624 (1998).
81. M. Das *et al.*, One-Pot Synthesis of Carboxymethyl-Dextran Coated Iron Oxide Nanoparticles (CION) for Preclinical fMRI and MRA Applications. *NeuroImage*, 118213 (2021).
82. F. Mandino *et al.*, Animal functional magnetic resonance imaging: trends and path toward standardization. *Frontiers in neuroinformatics* **13**, 78 (2020).
83. M. Fukuda, A. L. Vazquez, X. Zong, S. G. Kim, Effects of the α2□adrenergic receptor agonist dexmedetomidine on neural, vascular and BOLD fMRI responses in the somatosensory cortex. *European Journal of Neuroscience* **37**, 80-95 (2013).
84. N. Van Den Berge *et al.*, Functional circuit mapping of striatal output nuclei using simultaneous deep brain stimulation and fMRI. *Neuroimage* **146**, 1050-1061 (2017).
85. J. Paasonen, P. Stenroos, R. A. Salo, V. Kiviniemi, O. Gröhn, Functional connectivity under six anesthesia protocols and the awake condition in rat brain. *Neuroimage* **172**, 9-20 (2018).
86. S.-H. Lee *et al.*, An isotropic EPI database and analytical pipelines for rat brain resting-state fMRI. *Neuroimage* **243**, 118541 (2021).
87. J. Grandjean, A. Schroeter, I. Batata, M. Rudin, Optimization of anesthesia protocol for resting-state fMRI in mice based on differential effects of anesthetics on functional connectivity patterns. *Neuroimage* **102**, 838-847 (2014).
88. R. Gruetter, Automatic, localized in vivo adjustment of all first□and second□order shim coils. *Magnetic resonance in medicine* **29**, 804-811 (1993).
89. D. L. Albaugh *et al.*, Functional magnetic resonance imaging of electrical and optogenetic deep brain stimulation at the rat nucleus accumbens. *Scientific reports* **6**, 1-13 (2016).
90. K. Kazemi, H. A. Moghaddam, R. Grebe, C. Gondry-Jouet, F. Wallois, A neonatal atlas template for spatial normalization of whole-brain magnetic resonance images of newborns: preliminary results. *Neuroimage* **37**, 463-473 (2007).
91. N. Kriegeskorte, W. K. Simmons, P. S. Bellgowan, C. I. Baker, Circular analysis in systems neuroscience: the dangers of double dipping. *Nature neuroscience* **12**, 535-540 (2009).

Figures

Figure 1. Optogenetic stimulation of the AI with simultaneous fMRI in rats. (A) We applied feedforward optogenetic stimulation to neurons of the right AI during fMRI in Chronos-expressing rats (n = 9) and EYFP-expressing controls (n = 7), and extracted time-series data from ROIs corresponding to putative DMN and SN nodes. **(B)** Representative histological confirmation of EYFP viral vector expression (green) in the right AI (white) in coronal brain slices at 2.64 mm and 3.64 mm anterior to Bregma. (**C**) Optical fiber placement was confirmed by anatomical MRI to be within the right AI (green) between 2.64-3.64 mm anterior with respect to Bregma in both Chronos and EYFP-expressing rats. **(D)** Averaged AI response relative to optogenetic AI stimulation blocks in Chronos rats. **(E)** Averaged AI response relative to stimulation blocks in EYFP controls. Data are presented as mean and standard error of the mean. **(F)** Sagittal rat-brain cartoon highlighting regions of interest (ROIs) used for fMRI time-series extraction, comprising the right AI, Cg, prelimbic cortex PrL, and six subdivisions located at intervals of 1 mm along the anterior-posterior axis of the bilateral RSC, spanning from anterior RSC (aRSC) to posterior RSC (pRSC).

Figure 2. Overall data analysis approach for identifying AI-stimulation induced dynamic decoupling of the SN and DMN in rats. **(A, B)** We applied a novel BSDS model to time-series data extracted from individual ROIs corresponding to putative rat SN and DMN nodes to investigate brain state dynamics, and their temporal properties, associated with feedforward optogenetic stimulation of the AI. **(C)** We then examined dynamic changes in activation in each ROI and functional brain circuit connectivity associated with stimulation-related brain states.

Figure 3. Temporal properties of latent brain states associated with optogenetic stimulation of the AI in Chronos rats and EYFP controls. (A) Time-varying posterior probabilities of brain states identified in Chronos rats by the BSDS model across the AI stimulation protocol (top). Temporal evolution of the brain states identified in Chronos rats (bottom). **(B)** Time-varying posterior probabilities of the brain states in EYFP controls across the AI stimulation protocol (top). Temporal evolution of brain states identified in EYFP controls (bottom). **(C)** Classification analysis based on a linear Support Vector Machine classifier. Time-varying posterior probabilities of the latent brain states in Chronos rats distinguished stimulation ON and OFF blocks with a classification accuracy of 74.7%. In contrast, time-varying posterior probabilities of the latent brain states in EYFP controls distinguished the stimulation condition only at chance level (indicated by the black dashed line at 50%). Data are represented as mean and standard error of the mean. $*p < 0.05$, two-tailed *t*-test, FDR-corrected. **(D)** Occupancy rates of latent brain states in Chronos rats. The occupancy rate of State 1 was significantly higher during stimulation OFF blocks compared to stimulation ON blocks. In contrast, the occupancy rate of State 2 was significantly higher during stimulation ON blocks compared to stimulation OFF blocks. Data are represented as mean and standard error of the mean. $*p < 0.05$, two-tailed *t*-test, FDR-corrected. **(E)** Occupancy rates of brain states in EYFP controls. State 1 dominated both stimulation ON and stimulation OFF blocks. Data are represented as mean and standard error of the mean. $*p < 0.05$, two-tailed *t*-test, FDR-corrected. **(F)** Schematic illustrating

stimulation-dependent brain state dynamics in Chronos rats. Stimulation OFF blocks and stimulation ON blocks are dominated by State 1 and State 2, respectively.

Figure 4. Comparison of dynamic functional connectivity patterns in stimulation ON and OFF brain states in Chronos rats. (A, B) AI stimulation resulted in activation of AI and PrL and suppression of multiple subdivisions of the RSC in the ON, compared to the OFF, state (* $p < 0.05$, two-tailed *t*-test, FDR-corrected). **(C)** Specific links that showed significant differences in functional connectivity between the stimulation ON and OFF states (all *ps* < 0.05, two-tailed *t*-test, FDR-corrected). Functional connectivity significantly decreased between the AI and an anterior subdivision of the RSC (-2.90 mm AP), within the RSC (between subdivisions at -2.90 and -3.86, and at -6.86 mm AP), and between the PrL and a midRSC subdivision (–5.90 mm AP). Furthermore, functional connectivity increased between the PrL and Cg, and the PrL and posterior RSC (-7.82 mm AP). **(D-F)** Functional connectivity changes between AI, PrL, and posterior RSC (-6.86 mm AP) with other ROIs during the ON and OFF states (*$p < 0.05$, two-tailed *t*-test, FDR-corrected).

Figure 5. Identification and spatiotemporal properties of a Transition state in Chronos rats. (A) State switching probability of latent brain states at stimulation boundaries identified in Chronos rats. State switching probability is defined as the probability that a latent brain state at time instance (*t)* switches to other states at time instance (*t + 1)*, or remains in the same state. At the OFF→ON stimulation boundary, the switching probability from the OFF to ON state (i.e., $P_{OFF \rightarrow ON}$) was significantly lower than the switching probabilities from the OFF to State 3 (i.e., $P_{OFF \rightarrow State3}$) and from State 3 to the ON state (i.e., $P_{State3 \rightarrow ON}$), respectively (all *ps* < 0.001, two-tailed *t*-test, FDR-corrected). Furthermore, at the ON→OFF stimulation boundary, the switching probability from the ON to OFF state (i.e., $P_{ON \rightarrow OFF}$) was significantly lower than the switching probabilities from the ON state to State 3 (i.e., $P_{ON \rightarrow State3}$) and from the State 3 to OFF state (i.e., $P_{State3 \rightarrow OFF}$), respectively (all *ps* < 0.001, two-tailed *t*-test, FDR-corrected). **(B)** Analysis of state switching matrices revealed that state transitions between the OFF state (State 1) and the ON state (State 2) first passes through a Transition state (State 3) (** $p < 0.001$, two-tailed *t*-test). **(C)** Schematic illustrating the most likely state switching path from stimulation OFF to stimulation ON blocks.

Figure 6. Comparison of dynamic functional connectivity patterns of the Transition state with stimulation ON and OFF states in Chronos rats. (A, B) Regional activation levels during Transition and OFF states. AI stimulation resulted in a Transition state characterized by suppression of multiple anterior to mid-region RSC subdivisions, and activation of AI and multiple posterior RSC subdivisions (* $p < 0.05$, two-tailed *t*-test, FDR-corrected). **(C)** Specific links that showed significant differences in functional connectivity between Transition and OFF states (all *ps* < 0.05, two-tailed *t*-test, FDR-corrected). Functional connectivity between AI and posterior RSC (-5.8 mm AP) significantly increased, while connectivity within RSC decreased between anterior and posterior subdivisions in the transition state, compared to the stimulation

OFF state (all *ps* < 0.05, two-tailed *t*-test, FDR-corrected). **(D, E)** Regional activation levels during Transition and ON states. AI stimulation resulted in activation of AI, PrL, and Cg, and suppression of middle and posterior RSC (-5.8 and -6.8 mm AP) in the ON state, compared to the Transition state (**p* < 0.05, two-tailed *t*-test, FDR-corrected). **(F)** Specific links that showed significant differences in functional connectivity between the ON and Transition states (all *ps* < 0.05, two-tailed *t*-test, FDR-corrected). Functional connectivity significantly decreased between the AI and anterior RSC (-2.9mm AP), and between anterior-middle and posterior subdivisions within the RSC. Furthermore, functional connectivity increased between the PrL and Cg.

Tables

Table 1. Salience and default mode network nodes and their coordinates. Coordinates are based on the Paxinos and Watson rat brain atlas (6th edition) coregistered to a group-template MR image space and represent the center of mass for each ROI. A-P, D-V, and M-L indicate millimeters from the skull at Bregma in anterior–posterior, dorsal–ventral, and medial–lateral directions, respectively. M-L coordinates were positive to the right and negative to the left of the midline. ± denotes center of mass in each hemisphere for bilateral ROIs.

#	Region	Brain atlas coordinates		
		M-L	**D-V**	**A-P**
1	Prelimbic cortex (PrL)	±0.0	-3.3	+3.32
2	Anterior insular cortex (AI)	+3.8	-5.0	+3.32
3	Cingulate cortex (Cg)	±0.6	-2.4	+1.32
4	Retrosplenial cortex (RSC)	±0.6	-1.3	-2.90
5		±0.7	-1.3	-3.86
6		±0.8	-1.3	-4.86
7		±0.9	-1.3	-5.90
8		±1.0	-1.3	-6.86
9		±1.1	-1.3	-7.82

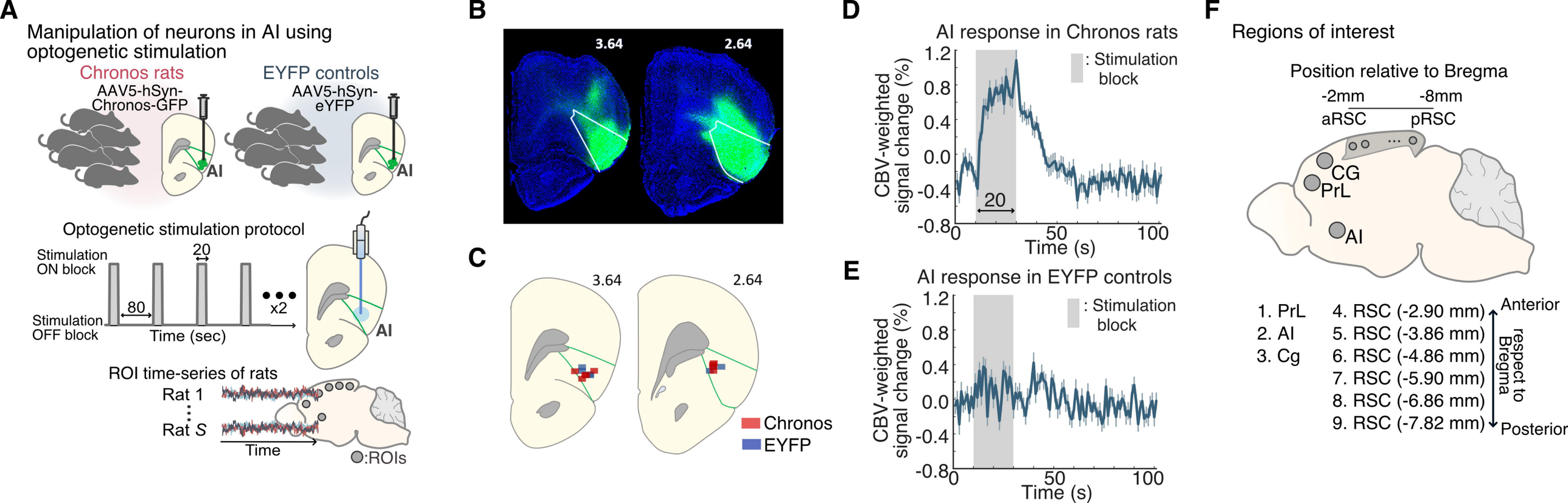
A
Manipulation of neurons in AI using optogenetic stimulation
Chronos rats
AAV5-hSyn-Chronos-GFP
EYFP controls
AAV5-hSyn-eYFP
AI
AI
Optogenetic stimulation protocol
Stimulation ON block
Stimulation OFF block
20
80
x2
Time (sec)
AI
ROI time-series of rats
Rat 1
Rat S
Time
:ROIs
B
3.64
2.64
C
3.64
2.64
Chronos
EYFP
D
AI response in Chronos rats
CBV-weighted signal change (%)
1.2
0.8
0.4
0.0
-0.4
-0.8
: Stimulation block
20
0
50
100
Time (s)
E
AI response in EYFP controls
CBV-weighted signal change (%)
1.2
0.8
0.4
0.0
-0.4
-0.8
: Stimulation block
0
50
100
Time (s)
F
Regions of interest
Position relative to Bregma
-2mm
-8mm
aRSC
pRSC
CG
PrL
AI
1. PrL
2. AI
3. Cg
4. RSC (-2.90 mm)
5. RSC (-3.86 mm)
6. RSC (-4.86 mm)
7. RSC (-5.90 mm)
8. RSC (-6.86 mm)
9. RSC (-7.82 mm)
Anterior
respect to Bregma
Posterior

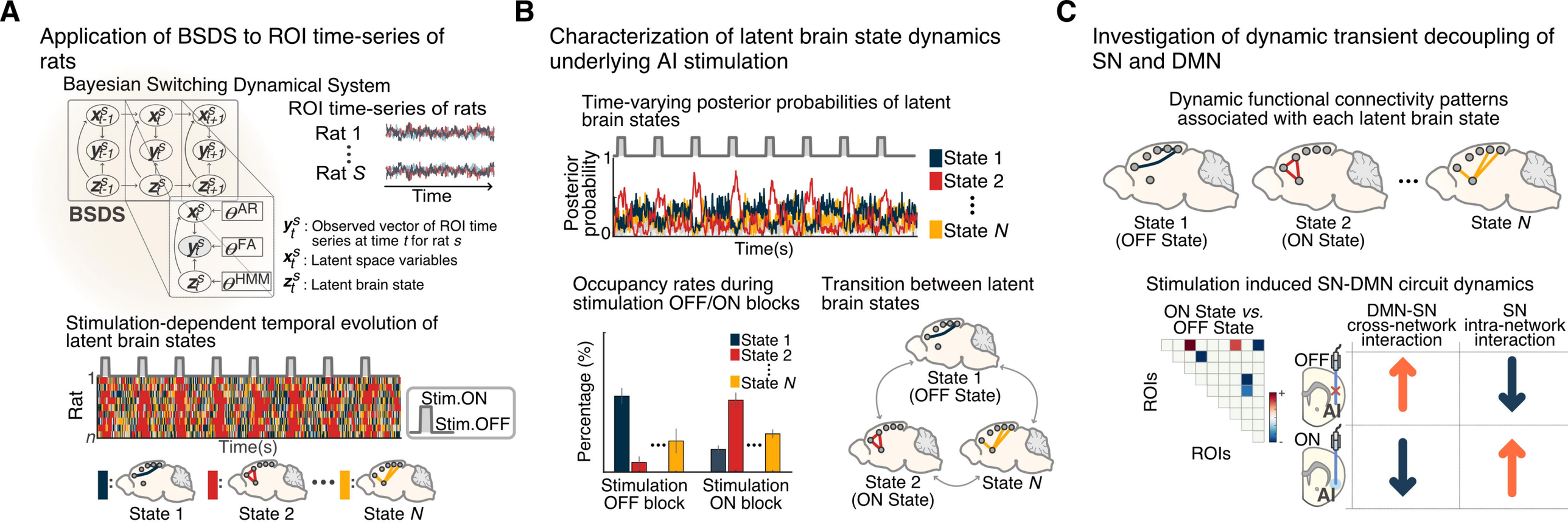
A
Application of BSDS to ROI time-series of rats
Bayesian Switching Dynamical System
BSDS
ROI time-series of rats
Rat 1
Rat S
Time
y_t^s : Observed vector of ROI time series at time t for rat s
x_t^s : Latent space variables
z_t^s : Latent brain state
Stimulation-dependent temporal evolution of latent brain states
Rat
Time(s)
Stim.ON
Stim.OFF
State 1
State 2
State N
B
Characterization of latent brain state dynamics underlying AI stimulation
Time-varying posterior probabilities of latent brain states
Posterior probability
Time(s)
State 1
State 2
State N
Occupancy rates during stimulation OFF/ON blocks
Percentage (%)
Stimulation OFF block
Stimulation ON block
Transition between latent brain states
State 1 (OFF State)
State 2 (ON State)
State N
C
Investigation of dynamic transient decoupling of SN and DMN
Dynamic functional connectivity patterns associated with each latent brain state
State 1 (OFF State)
State 2 (ON State)
State N
Stimulation induced SN-DMN circuit dynamics
ON State vs. OFF State
ROIs
ROIs
DMN-SN cross-network interaction
SN intra-network interaction
OFF
ON
AI
AI

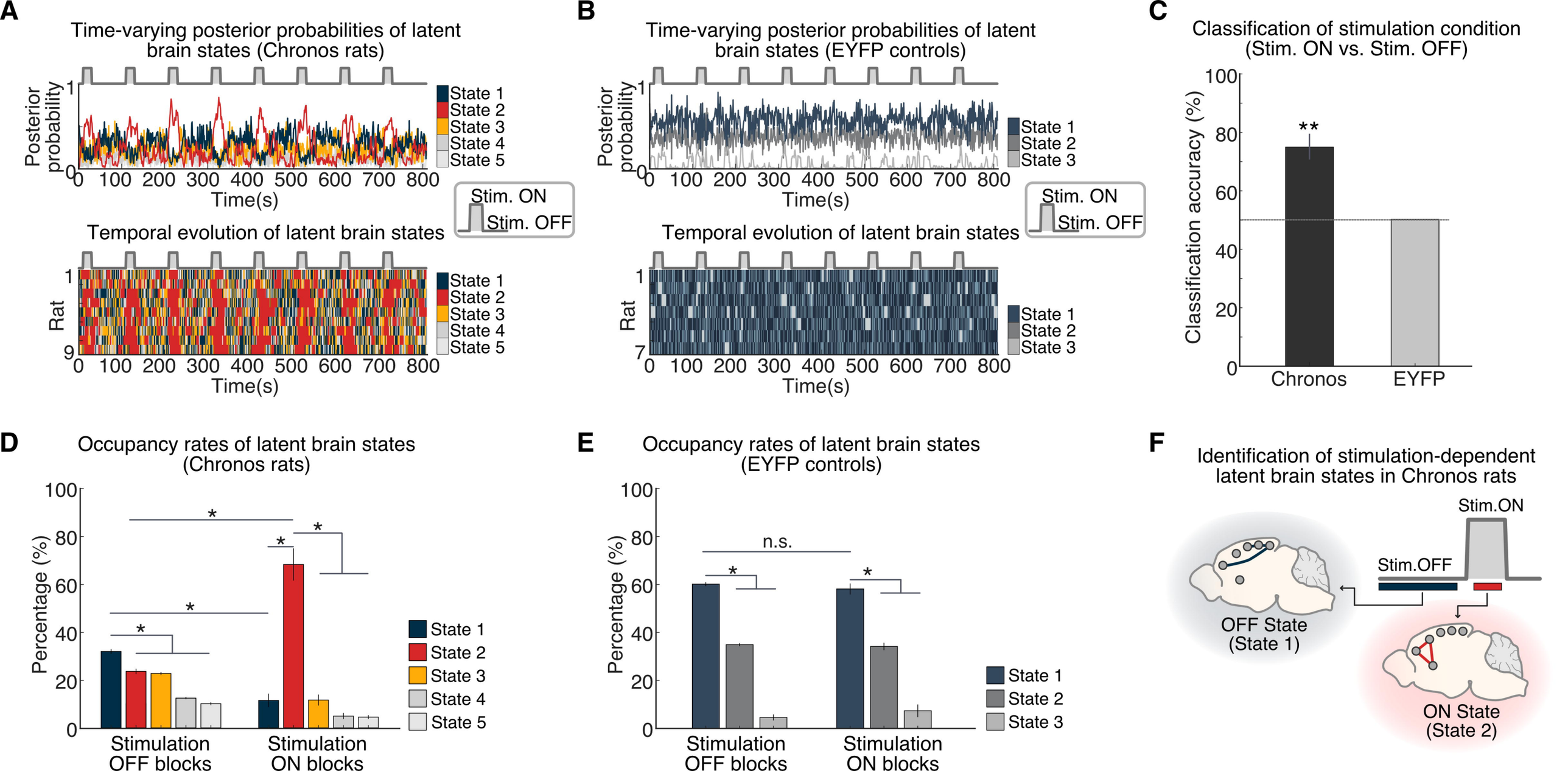
A
Time-varying posterior probabilities of latent brain states (Chronos rats)
Posterior probability
1
0
0 100 200 300 400 500 600 700 800
Time(s)
State 1
State 2
State 3
State 4
State 5
Stim. ON
Stim. OFF
Temporal evolution of latent brain states
Rat
1
9
0 100 200 300 400 500 600 700 800
Time(s)
State 1
State 2
State 3
State 4
State 5
B
Time-varying posterior probabilities of latent brain states (EYFP controls)
Posterior probability
1
0
0 100 200 300 400 500 600 700 800
Time(s)
State 1
State 2
State 3
Stim. ON
Stim. OFF
Temporal evolution of latent brain states
Rat
1
7
0 100 200 300 400 500 600 700 800
Time(s)
State 1
State 2
State 3
C
Classification of stimulation condition (Stim. ON vs. Stim. OFF)
Classification accuracy (%)
100
80
60
40
20
0
**
Chronos
EYFP
D
Occupancy rates of latent brain states (Chronos rats)
Percentage (%)
100
80
60
40
20
0
*
*
*
*
*
Stimulation OFF blocks
Stimulation ON blocks
State 1
State 2
State 3
State 4
State 5
E
Occupancy rates of latent brain states (EYFP controls)
Percentage (%)
100
80
60
40
20
0
n.s.
*
*
Stimulation OFF blocks
Stimulation ON blocks
State 1
State 2
State 3
F
Identification of stimulation-dependent latent brain states in Chronos rats
Stim.ON
Stim.OFF
OFF State (State 1)
ON State (State 2)

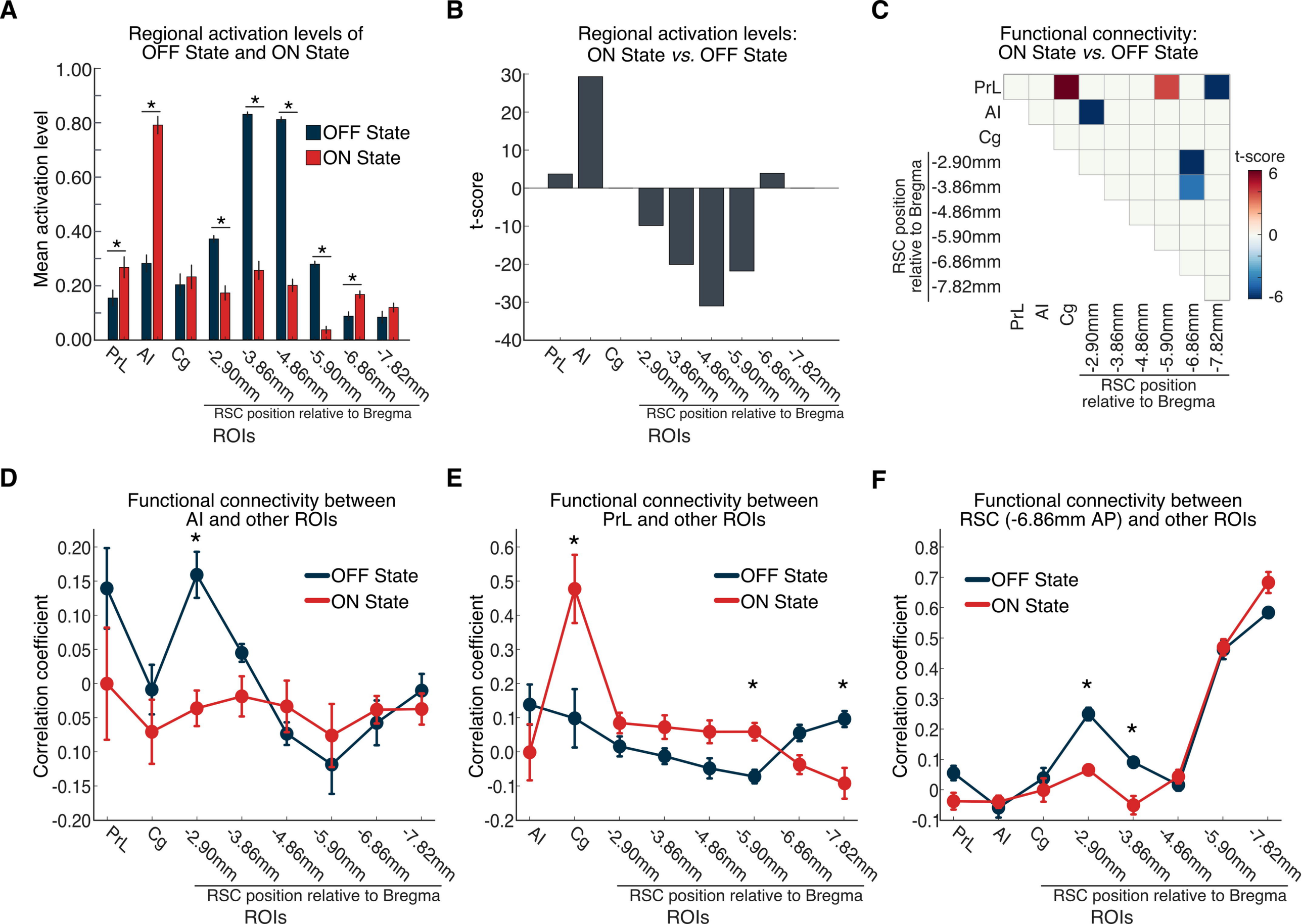
A
Regional activation levels of OFF State and ON State
Mean activation level
OFF State
ON State
PrL
AI
Cg
-2.90mm
-3.86mm
-4.86mm
-5.90mm
-6.86mm
-7.82mm
RSC position relative to Bregma
ROIs
B
Regional activation levels: ON State vs. OFF State
t-score
RSC position relative to Bregma
ROIs
C
Functional connectivity: ON State vs. OFF State
RSC position relative to Bregma
t-score
D
Functional connectivity between AI and other ROIs
Correlation coefficient
OFF State
ON State
RSC position relative to Bregma
ROIs
E
Functional connectivity between PrL and other ROIs
Correlation coefficient
OFF State
ON State
RSC position relative to Bregma
ROIs
F
Functional connectivity between RSC (-6.86mm AP) and other ROIs
Correlation coefficient
OFF State
ON State
RSC position relative to Bregma
ROIs

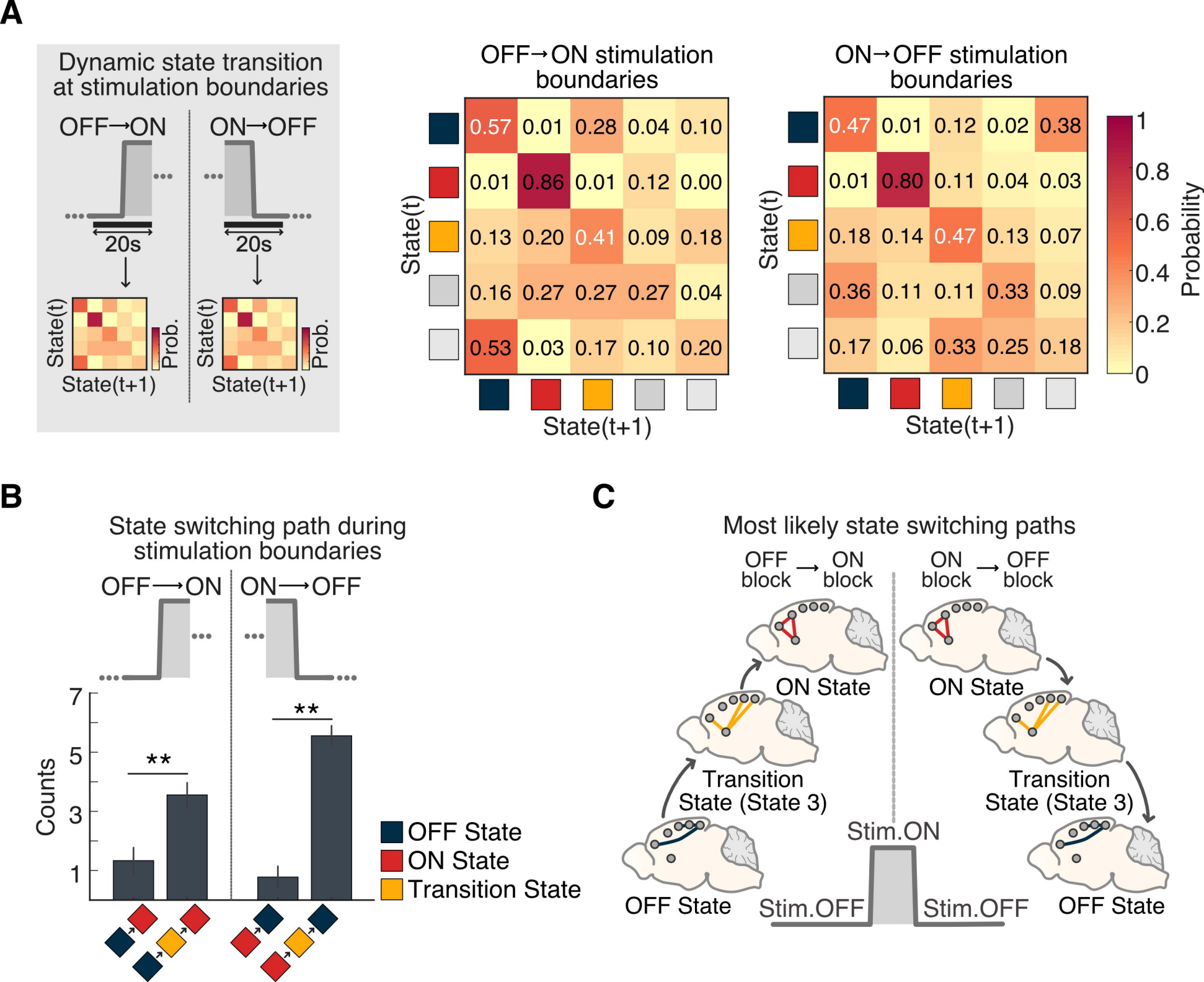
A
Dynamic state transition at stimulation boundaries
OFF→ON
ON→OFF
20s
20s
State(t)
State(t+1)
Prob.
OFF→ON stimulation boundaries
ON→OFF stimulation boundaries
0.57 0.01 0.28 0.04 0.10
0.01 0.86 0.01 0.12 0.00
0.13 0.20 0.41 0.09 0.18
0.16 0.27 0.27 0.27 0.04
0.53 0.03 0.17 0.10 0.20
0.47 0.01 0.12 0.02 0.38
0.01 0.80 0.11 0.04 0.03
0.18 0.14 0.47 0.13 0.07
0.36 0.11 0.11 0.33 0.09
0.17 0.06 0.33 0.25 0.18
State(t)
State(t+1)
Probability
1
0.8
0.6
0.4
0.2
0
B
State switching path during stimulation boundaries
OFF⟶ON
ON⟶OFF
Counts
7
5
3
1
**
**
OFF State
ON State
Transition State
C
Most likely state switching paths
OFF block ⟶ ON block
ON block ⟶ OFF block
ON State
ON State
Transition State (State 3)
Transition State (State 3)
Stim.ON
OFF State
Stim.OFF
Stim.OFF
OFF State

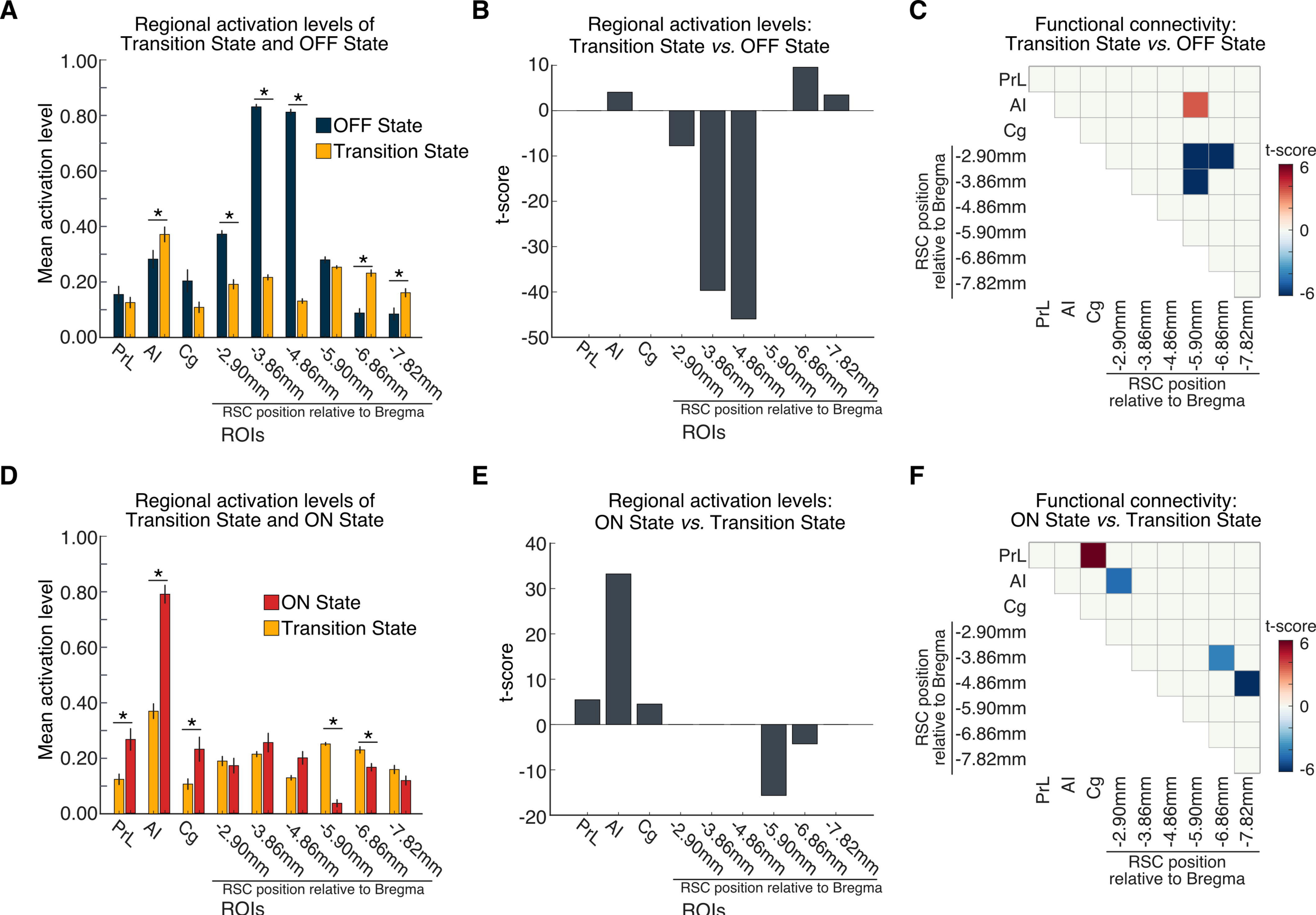
A
Regional activation levels of
Transition State and OFF State
Mean activation level
1.00
0.80
0.60
0.40
0.20
0.00
OFF State
Transition State
PrL
AI
Cg
-2.90mm
-3.86mm
-4.86mm
-5.90mm
-6.86mm
-7.82mm
RSC position relative to Bregma
ROIs
B
Regional activation levels:
Transition State vs. OFF State
t-score
10
0
-10
-20
-30
-40
-50
PrL
AI
Cg
-2.90mm
-3.86mm
-4.86mm
-5.90mm
-6.86mm
-7.82mm
RSC position relative to Bregma
ROIs
C
Functional connectivity:
Transition State vs. OFF State
PrL
AI
Cg
-2.90mm
-3.86mm
-4.86mm
-5.90mm
-6.86mm
-7.82mm
RSC position
relative to Bregma
t-score
6
0
-6
D
Regional activation levels of
Transition State and ON State
Mean activation level
1.00
0.80
0.60
0.40
0.20
0.00
ON State
Transition State
PrL
AI
Cg
-2.90mm
-3.86mm
-4.86mm
-5.90mm
-6.86mm
-7.82mm
RSC position relative to Bregma
ROIs
E
Regional activation levels:
ON State vs. Transition State
t-score
40
30
20
10
0
-10
-20
PrL
AI
Cg
-2.90mm
-3.86mm
-4.86mm
-5.90mm
-6.86mm
-7.82mm
RSC position relative to Bregma
ROIs
F
Functional connectivity:
ON State vs. Transition State
PrL
AI
Cg
-2.90mm
-3.86mm
-4.86mm
-5.90mm
-6.86mm
-7.82mm
RSC position
relative to Bregma
t-score
6
0
-6